JOURNAL OF SPACECRAFT AND ROCKETS
Vol. 46, No. 4, July–August 2009

# Hypersonic Turbulent Flow Simulation of FIRE II Reentry Vehicle Afterbody

D. Siva K. Reddy* and Krishnendu Sinha†
*Indian Institute of Technology Bombay, Mumbai 400 076, India*

DOI: 10.2514/1.41380

**This paper presents a numerical investigation of the hypersonic reacting flow around the FIRE II reentry capsule. At the chosen freestream conditions, the forebody boundary layer and the separated flow on the afterbody are turbulent. The Reynolds-averaged Navier–Stokes method along with two commonly used turbulence models are used to compute the flowfield. Accurate prediction of turbulent separated flow at hypersonic conditions is challenging due to the limitations of the underlying turbulence models. The presence of turbulent eddy viscosity in the flow simulation results in a smaller separation bubble than the laminar solution at identical conditions. Also, the two turbulence models predict different levels of eddy viscosity in the neck region. This has a dominant effect on the separation bubble size and the surface pressure. On the other hand, the eddy viscosity values in the near-wall region determine the heat transfer rate to the body. The two models predict comparable heating rates on the conical frustum, and the results match in-flight measurement well. By comparison, surface pressure predictions are appreciably higher than the data.**

## Nomenclature

$D$ = diameter of the vehicle, m
$k$ = turbulent kinetic energy, J/kg
$M$ = Mach number
$p$ = pressure, Pa
$q$ = heat transfer rate, $\mathrm{W/cm^2}$
$Re_D$ = Reynolds number based on freestream conditions and body diameter
$s$ = arc length from the nose stagnation point, m
$T$ = translational-rotational temperature, K
$T_v$ = vibrational temperature, K
$U$ = velocity, m/s
$\mu$ = molecular viscosity, $\mathrm{Pa \cdot s}$
$\mu_T$ = turbulent eddy viscosity, $\mathrm{Pa \cdot s}$
$\nu_T$ = turbulent kinematic viscosity, $\mathrm{m^2/s}$
$\rho$ = density, $\mathrm{kg/m^3}$
$\omega$ = specific turbulent dissipation rate, 1/s

*Subscripts*

$T$ = turbulent
$w$ = wall
$\infty$ = freestream

## I. Introduction

ATMOSPHERIC reentry vehicles are subjected to large aerothermal loads, which play an important role in their design and operation. During the later part of their descent, the flow around the vehicle, especially in the wake region, transitions to turbulence. This can significantly increase the heat transfer to the vehicle walls. Predicting turbulent heating rate is challenging due to the uncertainties in the turbulence models. Flow separation on the afterbody typically accentuates these uncertainties. As a result, a large safety factor is generally used in the design of afterbody heat shields [1].

Wright et al. [1] present a comprehensive compilation of available aeroheating measurements on reentry capsule configurations, with the focus on afterbody flowfield. Flight data show that there is enhanced heating on portions of the afterbody in several cases such as Gemini, Mercury, and Apollo, which may be attributed to transition to turbulence. In another recent review, Schneider [2] highlights the effects of transition on reentry capsule flowfields using data collected from flight and ground tests. Several afterbody flow features, including separation and reattachment locations, and the associated heating rates show a strong dependence on whether the flow is laminar or turbulent.

Of all the reentry flight and ground tests listed in [1,2], only a few have been investigated using modern computational fluid dynamics (CFD) methods. Most notably, the FIRE II and Apollo AS-202 flowfields are computed at a series of time points spanning their respective heat pulses. The axisymmetric simulation of the zero-angle-of-attack FIRE II configuration matches the experimental data well [3]. Similarly, computation of the three-dimensional flowfield around the AS-202 vehicle yields heat transfer rates that are within the scatter of in-flight measurements [4]. However, the majority of the trajectory points considered in [3,4] have Reynolds numbers low enough for the flow to be laminar. The only exception is the AS-202 data during the second heat pulse, in which laminar calculations underpredict the heating measurements. Fully turbulent predictions are higher than data, which indicate possible transitional flow at these conditions. Thus, CFD validation for turbulent flow around reentry vehicles is very sparse in literature, and further work is required to understand and accurately predict turbulent reentry wake flows [1].

The ground-based tests of the Crew Exploration Vehicle (CEV) configuration [5] achieved significantly higher Reynolds numbers than flight conditions. Transition to turbulence occurred on the forebody surface, and computational predictions are found to reproduce the extensive heat transfer rate measurements. Much of the experimental and computational effort is directed toward the forebody analysis, with limited data available on the afterbody. In another investigation, Brown [6] computed the flow around a sphere-cone geometry with heat transfer measurements on the model afterbody and sting. The flow was found to transition at reattachment on the sting, and several turbulence models were evaluated against the experimental data. Although the findings are relevant to reentry wake flow prediction, it is not clear how the presence of a sting affects the recirculating flow and the resulting afterbody pressure and heat

---

Presented as Paper 805 at the 45th Aerospace Sciences Meeting and Exhibit, Reno, NV, 8–11 January 2007; received 6 October 2008; revision received 31 March 2009; accepted for publication 2 April 2009.

*Doctoral Student, Department of Aerospace Engineering.

†Assistant Professor, Department of Aerospace Engineering. Member AIAA.

transfer rate. Therefore, it is desirable to validate turbulence model predictions against in-flight afterbody measurements, which do not have any sting-interference effect. The current work is a step in this direction.

We study the transitional/turbulent flow around the FIRE II reentry vehicle. The Reynolds number at the conditions considered here is more than twice of the highest value considered for AS-202 [4]. Transition to turbulence is therefore expected to occur earlier on the vehicle than in the Apollo case, possibly even on the forebody. The objective of the current work is to compute the reacting turbulent hypersonic flow around the FIRE II reentry module using Reynolds-averaged Navier–Stokes (RANS) equations and to evaluate the accuracy of the aerothermal predictions against in-flight measurements. The effects of turbulence on the gas properties are studied by comparing the RANS solution with the results of a laminar simulation at identical conditions. Furthermore, variation between commonly used turbulence models is presented in terms of their eddy viscosity distribution in the flowfield. The resulting effect on the mean flow structure and the corresponding difference in the aerothermal predictions are discussed in detail.

The paper is organized as follows. A brief outline of the FIRE II vehicle geometry and the associated physical flow phenomena are presented subsequently. The simulation methodology and the grid generation technique are discussed next. The grid is carefully refined and adapted to the prominent flow features to ensure accurate prediction of the flowfield. Results include a description of turbulent flowfield solution and surface properties such as pressure and heat transfer. This is followed by comparison of turbulent vs laminar computations. Finally, variation between commonly used turbulence models and the effect of compressibility corrections are presented, followed by their comparison with flight data.

## II. FIRE II Configuration

Project FIRE (Flight Investigation Reentry Experiment) flights [7] were conducted to investigate the heating environment on a blunt-nosed Apollo-shaped vehicle entering the Earth's atmosphere at a velocity in excess of the escape velocity. Figures 1a and 1b, taken from [7], show a schematic of the FIRE II vehicle. The spherical forebody consisted of a multilayer configuration made of three protective phenolic asbestos heat shields sandwiched between three beryllium calorimeters. The first two calorimeters and their associated heat shields were jettisoned during the flight at predetermined deceleration loads. The third heat shield was not ejected, and this gives the shape of the vehicle through the later part of the reentry that is of interest in this work. The outer mold line used in the current simulations is shown in Fig. 1c. The vehicle diameter is 58.79 cm with a nose radius of 70.2 cm. The shoulder/corner radius is 0.61 cm and the base radius is 4.2 cm. The afterbody is conical with a 66 deg included angle, and the C-band antenna at the base is replaced by a flat base, for simplicity. Also, geometrical details at the heat-shield/aftshell junction and the ringlike structure at the base are not considered in the outer mold line presented in Fig. 1c. Their effect on the flow structure is studied separately in Sec. IV.D.

The FIRE II vehicle entered Earth atmosphere at 11.2 km/s. It decelerated to a velocity of 4950 m/s (Mach 16) at 35 km altitude. Slocumb [7] presents the time history of altitude and velocity over the entire descent. We simulate the conditions (listed in Table 1) at the 35 km trajectory point, which corresponds to one of the lowest altitudes and highest Reynolds numbers for which measurements are available. The Reynolds number based on freestream conditions and body diameter is $1.76 \times 10^6$. Blunt-body separation shear layer and inner wake transition correlations are presented by Lees [8]. A transition criteria is defined in terms of the Reynolds number computed using local flow properties outside the wake. The distance measured along the shear layer, starting from the separation point, is used as the relevant length scale to identify the physical location at which the Reynolds number approaches the transitional range. Based on these correlations and data from preliminary simulations of the FIRE II configuration, the wake is expected to transition upstream of the neck.

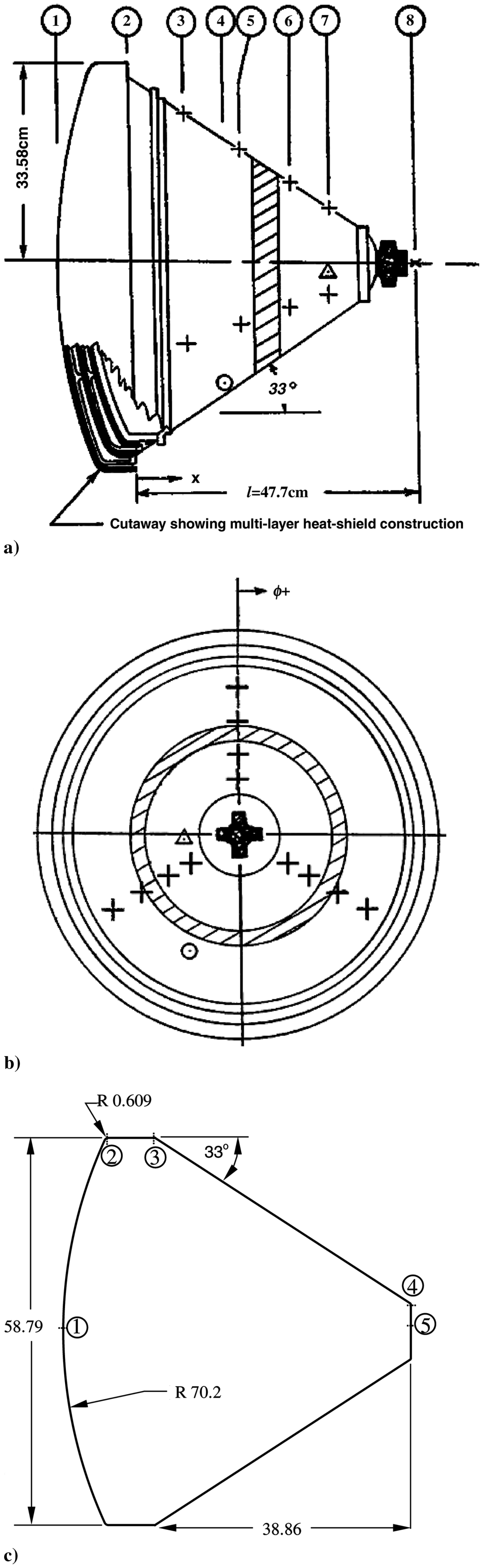

**Fig. 1 FIRE II reentry vehicle with afterbody instrumentation [7]: a) side view b) rear view (+, △, and ⊙ represent gold calorimeters, pressure sensor, and radiometer, respectively) and c) outer mold line used for the current simulations. All dimensions are in centimeters. Critical geometrical points are 1) fore stagnation point $s/D = 0$, 2) fore shoulder $s/D = 0.51$, 3) heat-shield/backshell interface $s/D = 0.64$, 4) aft shoulder $s/D = 1.42$, and 5) aft stagnation point $s/D = 1.49$.**

**Table 1 Freestream conditions for the current FIRE II simulations**

| Freestream conditions | Values |
|---|---|
| Altitude, km | 35 |
| Time from launch, s | 1652.75 |
| $\rho_\infty$, kg/m$^3$ | 0.0082 |
| $U_\infty$, m/s | 4950 |
| $T_\infty$, K | 237 |
| $M_\infty$ | 16 |
| $Re_D$ | $1.76 \times 10^6$ |

The vehicle afterbody was instrumented for pressure and surface temperature measurements. Pressure was measured at a single location and 12 gold calorimeters were placed at four axial locations along three circumferential rays ($\phi = 0$, 120, and 240 deg). Here, $\phi$ denotes the azimuthal angle around the vehicle, as shown in Fig. 1b. The system accuracy, including that of sensors and telemetry system, was approximately $\pm 20\%$ for the pressure data and about $\pm 28$ K for the temperature measurements. The corresponding error in heat transfer measurement is estimated to be $\pm 15\%$ [3]. The surface temperature measured by the calorimeters is presented as a function of reentry elapsed time. From this temperature-time history, an average wall temperature of 553.3 K is taken at 35 km altitude. In the later part of the trajectory the vehicle has periodic motion about its axis, resulting in oscillations in the effective angle of attack. However, there is negligible effect of angle-of-attack variation on the afterbody measurements, with no appreciable difference between the heating rates along the three circumferential rays [7]. The angle of attack is therefore assumed to be zero in the current simulations.

## III. Simulation Methodology

The chemically reacting turbulent hypersonic flow around the FIRE II reentry configuration is simulated by solving the Reynolds-averaged Navier–Stokes (RANS) equations along with the species conservation equations and a thermal nonequilibrium model. The freestream total enthalpy at the current condition (12.73 MJ/kg) is similar to that of Apollo AS-202 computations in [4], in which ionization is found to be negligible. Hence, air is modeled as a neutral mixture of five perfect species ($N_2$, $O_2$, NO, N, and O) with three dissociation and two exchange reactions. Rotational modes of the molecules are assumed to equilibriate with the translational modes and are described by a translational-rotational temperature $T$. Vibrational modes are represented by a separate vibrational temperature $T_v$ [9]. An additional conservation equation is solved for the vibrational energy of the mixture to account for the thermal nonequilibrium. The vibrational relaxation source term is calculated using Landau–Teller formulation based on a harmonic oscillator model for diatomic molecules [10]. The Arrhenius rate constants for the chemical reactions are evaluated using curve fits to experimental data by Park [9].

The $k$-$\omega$ model of Wilcox [11] and the Spalart–Allmaras (SA) model [12] are used for turbulence closure. The standard forms of the turbulence models, without compressibility corrections, are used in the majority of the work. The effect of compressibility corrections is discussed separately. Chemical and vibrational source terms are evaluated using mean flow properties, such that effect of turbulence-chemistry interaction is neglected. The molecular viscosity of each species is determined using curve-fit data of Blottner et al. [13]. Thermal conductivities for the translational and rotational modes of the species are then determined using the Eucken relation [14]. Viscosity and thermal conductivity of the mixture are computed using Wilke's mixing rule [15]. Palmer and Wright [16] show that Wilke's mixing rule is a good approximation for computing the mixture viscosity if the shock layer temperature is below ionization limits. Multicomponent mass diffusion due to concentration gradient is modeled using Fick's law with a Lewis number of 1.4. Turbulent transport of heat and mass are computed using a turbulent Prandtl number of 0.9 and a turbulent Lewis number of 1.0, respectively.

The axisymmetric form of the governing equations are discretized using the finite volume approach. Inviscid fluxes are computed using a modified (low-dissipation) form of the Steger–Warming flux-splitting approach [17], and the turbulence model equations are fully coupled to the mean flow equations [18]. The method is second-order-accurate in both streamwise and wall-normal directions. The viscous fluxes and the turbulent source terms are evaluated using second-order-accurate central differencing, and the implicit data-parallel line relaxation method [19] is used to obtain steady-state solutions.

No-slip, noncatalytic, and isothermal boundary conditions are specified at the wall. The boundary conditions for the $k$-$\omega$ turbulence model are as per Menter's recommendations [20]. In the freestream, $\omega_\infty = 10U_\infty/D$ and $k_\infty = 0.01\nu_\infty\omega_\infty$, where $D$ is chosen as the characteristic length dimension for the current configuration. At the wall, $k_w = 0$ and $\omega_w = 6\nu_w/\beta y_2^2$, where $y_2$ is the distance between first grid point and wall, and $\beta = 3/40$ is a model constant. For the SA turbulence model, boundary conditions are $\nu_{T\infty} = 0.1\mu_\infty/\rho_\infty$ and $\nu_{T,w} = 0$, as given in [12]. Freestream conditions are applied at the outer boundary, and the extrapolation boundary condition is imposed at the exit station. The simulation results are found to be insensitive to the specific values of $k$, $\omega$, and $\nu_T$ prescribed in the freestream.

A typical grid used in the simulations is shown in Fig. 2. The outer boundary follows the shape of the bow shock and extends up to 2.5 diameters downstream of the vehicle base. The flow at this point is found to be supersonic, and therefore the location of the exit boundary is not expected to alter the flow solution in the vicinity of the vehicle. A typical grid consists of about 160 points in the wall-parallel direction $i$ and 150 points in the wall-normal direction $j$. Grids with a larger number of points are also used in some cases.

The forebody grid in the $i$ direction is designed such that points are clustered in the nose stagnation region and at the shoulder expansion corner. The grid in the $j$ direction is refined both in the vicinity of the shock wave and in the near-wall region. In addition, the outer boundary is carefully tailored to the bow shock wave. The forebody grid refinement follows the same procedure as delineated in [21], and details are omitted for the sake of brevity. The current paper is focused on the afterbody solution, and a careful grid refinement in the afterbody region is presented subsequently.

### A. Afterbody Grid Refinement Study

A careful grid refinement study is undertaken for the afterbody flowfield by identifying the critical regions, in which the flow solution is most sensitive to the computational mesh. The grid is successively refined with a focus on the critical zones, and the grid lines are adapted to the prominent flow features such as the free shear layer enclosing the recirculation bubble. The effect of grid changes on the afterbody surface pressure and heating rate is studied, and a tolerance of 2% of the base stagnation-point value is taken as the

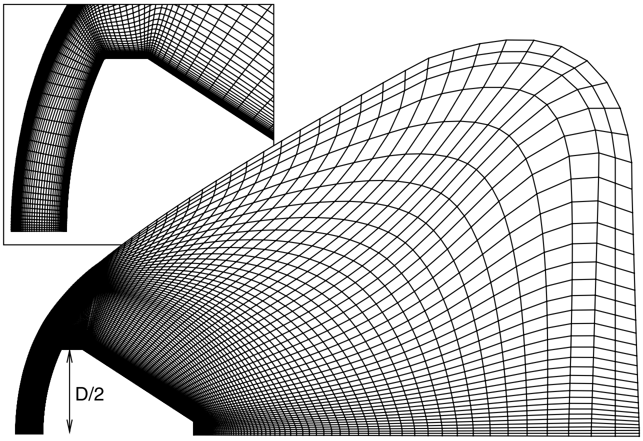

**Fig. 2 Computational domain and a typical grid used in the simulations. The inset shows a magnified view of the grid near the vehicle, where every second point is shown in each direction.**

grid-independence criterion. Figures 3 and 4 show the results from the grid refinement study using the SA turbulence model, in which pressure, normalized by its freestream value, and heat transfer rate are plotted as a function of the normalized arc length $s/D$ measured from the nose of the vehicle. The extent of conical frustum and flat base are marked by vertical lines.

Afterbody flowfield is sensitive to the distribution of grid points and the quality of the computational mesh in regions in which the flow gradients are high. In the wall-parallel direction, for example, these correspond to the geometric corners, stagnation point at the base, and the separation point on the conical frustum. Zonal grid refinement in these regions is done to identify the most critical requirements. It is found that a fine grid near the separation point along with a low stretching factor on the conical frustum is necessary for grid convergence. The results are, however, not so sensitive to the grid spacing at the rear stagnation point and the expansion corner at the base. Three grids with successive refinement along the conical frustum, especially near the separation point, are used to compute the flow, and the results are presented in Fig. 3. The two finer grids ($240 \times 171$ and $280 \times 171$) yield practically identical (within 1%) pressure and heat transfer results on the afterbody. A total of 240 points in the wall-parallel direction is therefore taken to be adequate for a grid-independent solution.

In the wall-normal direction, special attention is given to the accurate resolution of the free shear layer enclosing the recirculation bubble. Three grids ($160 \times 150$, $160 \times 171$, and $160 \times 220$) with successive refinement in the $j$ direction are used to compute the flow. The majority of the refinement is localized in the free shear layer and the recirculation bubble. The velocity distribution across the shear layer (see Fig. 5) shows almost overlapping results from the two finer grids. The pressure and heating rates obtained on the three grids are also comparable, with negligible difference between the two finer grids (Fig. 4). A total of 171 points is therefore taken to be adequate in the wall-normal direction.

Further, the computational mesh in the near wake is modified such that the grid lines are parallel to the shear layer. This is done by identifying a separate grid block enclosing the recirculation bubble and the shear layer (see Fig. 6) and carefully controlling the distribution of points along the block boundaries. The shear-layer-adapted grid yields a practically identical size of separation bubble and shear layer location compared with the baseline grid (bottom half of Fig. 6). The surface pressure and heating rate show negligible difference between the results computed on the two grids (see Fig. 7).

Based on the foregoing study, the $240 \times 171$ baseline grid was finalized, and all results using SA model presented subsequently are computed on this grid. A similar grid refinement study was undertaken for the $k$-$\omega$ model, but is not presented here.

All of the grids presented previously for the SA model have a wall-normal spacing of $10^{-6}$ m on the entire vehicle. This is equivalent to $y^+$ of 0.9 or less along the forebody attached boundary layer and 0.02 or less on afterbody. Further refinement is found to have negligible (less than 0.2%) effect on the heat transfer rate obtained using the SA model. The $k$-$\omega$ turbulence model requires finer grid at the wall and is discussed later.

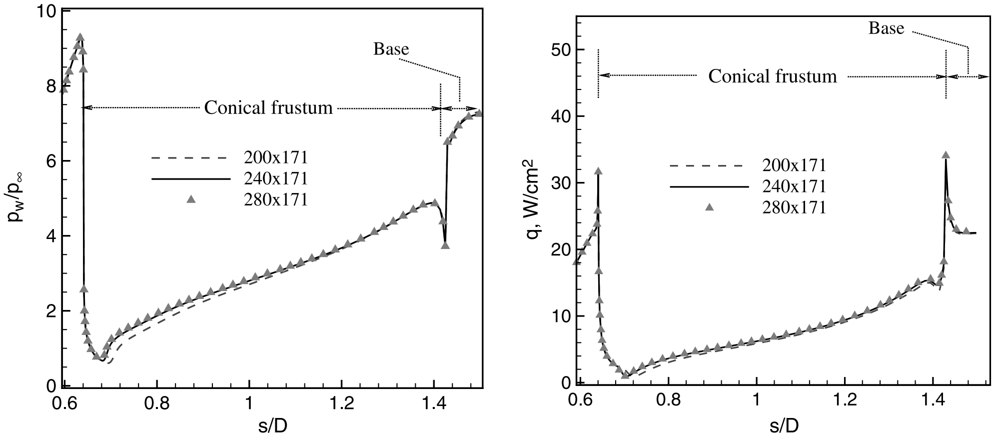

a) b)

**Fig. 3 Plots of a) normalized pressure and b) heat transfer rate on the afterbody computed using successively refined grids in the wall-parallel direction.**

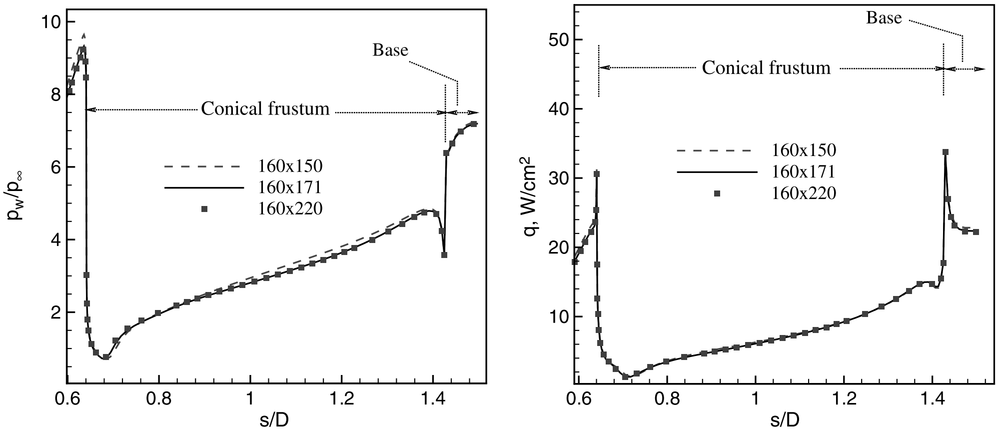

a) b)

**Fig. 4 Plots of a) normalized pressure and b) heat transfer rate on the afterbody computed using successively refined grids in wall-normal direction.**

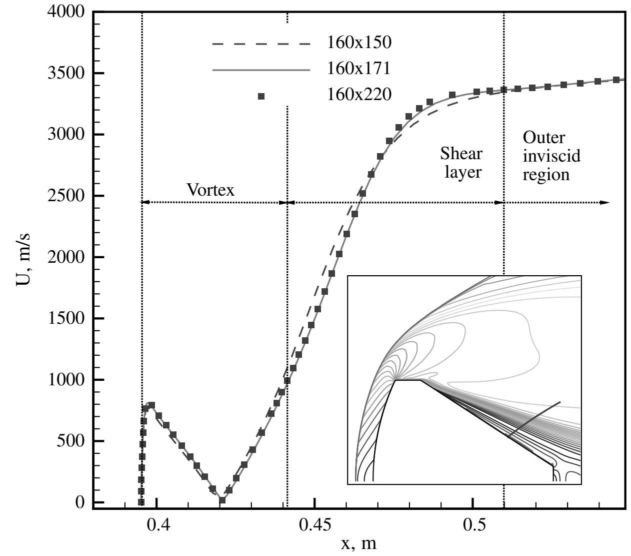

**Fig. 5 Effect of wall-normal grid refinement on velocity distribution across the free shear layer. Data are plotted along the line shown in the inset.**

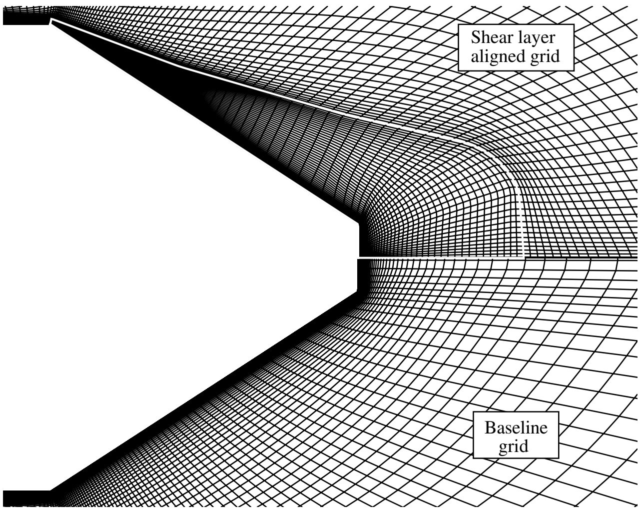

**Fig. 6 Grid-point distribution in the baseline grid (bottom half) and a modified grid that is adapted to the shear layer (top half). White line identifies the boundary of the grid block enclosing the shear layer and separation bubble.**

## B. Iterative Convergence

The flowfield is initialized to freestream values, except for a small region next to the conical afterbody and flat base, in which the velocity is set to zero. The advancement of the solution is studied in terms of flow feature development and the corresponding residual history. The rms density residual, normalized by its initial value, is plotted in Fig. 8 as a function of the number of time steps. The corresponding physical time, normalized by $\tau_f$, is discussed subsequently. The characteristic flow time $\tau_f$ is defined as $\tau_f = D/U_\infty$, and is $1 \times 10^{-4}$ s for the current configuration.

There is a rapid drop in the residual for the first 20,000 time steps. This corresponds to the development of the bow shock and the boundary layer on the forebody and to the expansion fans at the shoulder. The flow on the forebody reaches steady state during this period, which corresponds to about 12 $\tau_f$. The separation bubble starts forming at this time and it grows to its full size by about 46 $\tau_f$. The recirculating flow in the near wake shows a very slow convergence to the steady state and it takes up to $2 \times 10^5$ iterations at a Courant–Friedrichs–Levy number of 100 to arrive at the final solution.

Beyond the initial drop, the rms residual continues to fluctuate between $2 \times 10^{-5}$ and $10^{-4}$. These fluctuations correspond to a grid point located along the bow shock near the first expansion corner on the shoulder. This may be caused by a slight misalignment of the shock with the grid lines. There is, however, no noticeable change in the shock location or shape at this point, and the large value of the local residual does not appear to affect the rest of the flowfield.

The high local residual value at the bow shock misalignment point masks the iterative convergence of the afterbody flowfield after the first 50,000 time steps. A second rms residual is therefore computed in the region downstream of the shoulder and is referred to as the *afterbody residual* in Fig. 8. Compared with the full-domain residual, the afterbody residual drops to a lower value, but oscillates around $2.5 \times 10^{-7}$. The origin of these oscillations is traced to the separation point on the conical frustum. In the vicinity of separation point, all the flow variables are found to fluctuate with very small amplitude (less than 0.05% of the mean). The location of the separation point is not altered, however, and therefore these oscillations have negligible effect on the remainder of the flowfield. This can be seen from the residual computed only in the region downstream of the separation point, denoted by the wake residual in Fig. 8. This includes the majority of the recirculation bubble, the neck region, and the far wake. The wake residual shows a steady drop to about $3 \times 10^{-9}$ after $2.5 \times 10^5$ time steps. The iterative convergence of the afterbody heating rate to its steady-state value is shown in Fig. 9. There is no noticeable difference between the heat transfer rates obtained after $2 \times 10^5$ and $2.5 \times 10^5$ time steps, and this is taken as an indicator for terminating the time-iteration process.

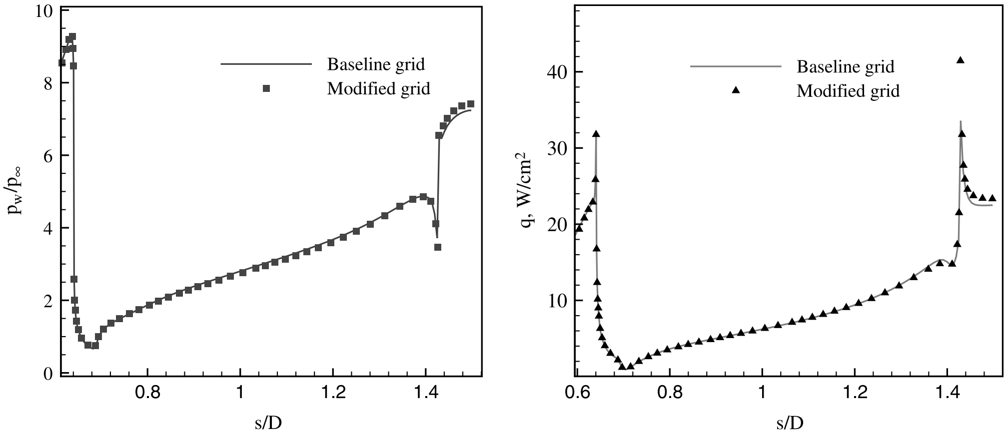

a) b)

**Fig. 7 Plots of a) normalized pressure and b) heat transfer rate on the afterbody computed using the baseline grid and a modified grid that is adapted to the shear layer.**

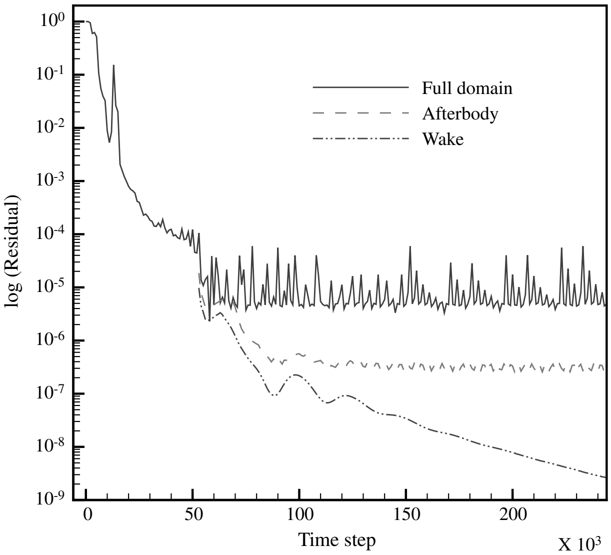

**Fig. 8 Residual history for a typical simulation. Full-domain indicates the rms residual in the entire computation domain, afterbody refers to the rms residual in the afterbody domain, and wake residual corresponds to the afterbody region of the grid downstream of the separation point.**

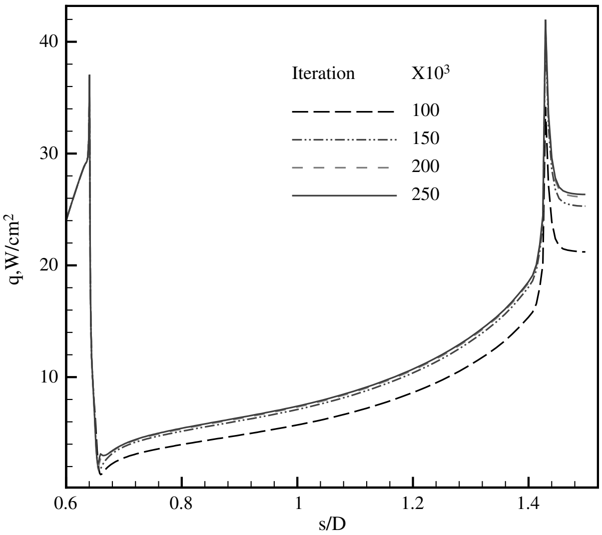

**Fig. 9 Afterbody heat transfer rate after different time steps.**

Overall, it typically requires computing over 220 $\tau_f$ to reach the final steady-state solution for the current FIRE II flowfield. For a 240 × 171 grid, this takes about 230 CPU hours on a 2.6 GHz Intel-processor-based machine.

## IV. Results

Figure 10 shows the RANS solution computed using the SA turbulence model in terms of the Mach number contours. The prominent features such as bow shock and flow expansion at the corners can be easily identified. The flow on the entire forebody is subsonic, with Mach number approaching unity close to the first expansion corner. The boundary layer remains attached through the two successive expansions and separates downstream of the second corner. Flow separation on the conical frustum is found to generate a mild lip shock. The recirculation bubble on the afterbody is characterized by a single toroidal vortex that extends up to about 0.36 diameters downstream of the base. The shear layer enclosing the recirculation region coalesces at the neck and a recompression shock wave is generated. The flow is subsonic in the recirculation bubble, and it expands to supersonic Mach numbers downstream of the neck.

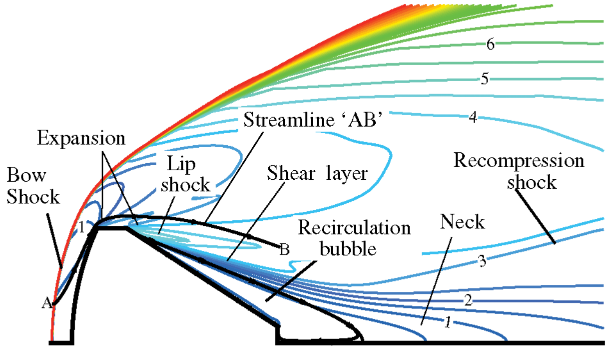

**Fig. 10 Mach number distribution in the turbulent (SA model) flowfield around the FIRE II reentry capsule at Mach 16 and 35 km altitude. Representative streamlines are shown to identify the recirculation bubble.**

The postshock temperature in the fore stagnation region is about 5700 K and it varies less than 5% on the forebody. At this temperature oxygen is completely dissociated, whereas nitrogen is mostly in its molecular form. There is a small amount of NO formed in this region. Isothermal condition drops the temperature to 553.3 K at the wall, causing recombination of oxygen atoms in the boundary layer. The rapid drop in fluid density associated with the expansion process leads to a frozen thermochemical state of the gas. The gas composition on the afterbody is approximately the same as that in the forebody inviscid region.

Figure 11 plots the translational-rotational and vibrational temperatures of the gas mixture along a stream line (identified in Fig. 10) passing through the bow shock and the inviscid regions on the forebody, shoulder, and afterbody. The two temperatures are identical in the postshock flow on the forebody. As the gas expands around the shoulder, the vibrational temperature freezes at about 5000 K, whereas the translational-rotational temperature drops to values lower than 2000 K. In the recirculation bubble, the translational temperature gets elevated due to viscous and turbulent dissipation, with values exceeding $T_v$ by about 350 K. Thus, the gas goes from a thermal equilibrium state on the forebody through a nonequilibrium region on the shoulder to a thermally frozen state on the afterbody.

The thermal nonequilibrium in the flow is computed using a two-temperature model. If a thermal equilibrium state is assumed, a single temperature ($T = T_v$) can be used to characterize the translational, rotational, and vibrational energy modes of the molecules. The value of $T$ thus computed using thermal equilibrium is found to be

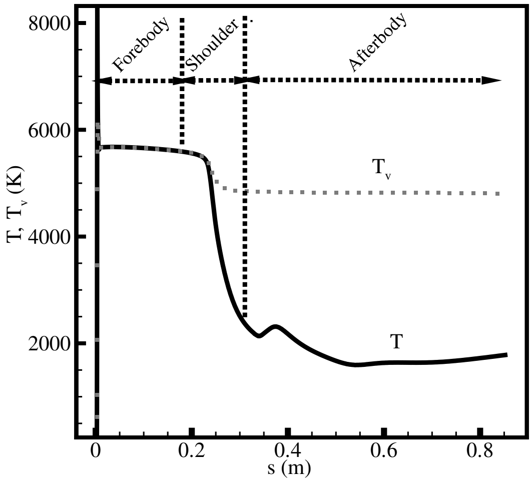

**Fig. 11 Variation of the translational-rotational and vibrational temperatures along a streamline (identified as streamline AB in Fig. 10) that passes through the bow shock wave, forebody and afterbody expansion regions.**

comparable with that obtained using the two-temperature model in a majority of the flowfield. The only exception is the inviscid expansion region around the shoulder, in which there is a large difference between the two temperatures. In the separation bubble, assuming thermal equilibrium does not alter the temperature level by more than 5% of the values computed using the two-temperature model. The resulting effect on the afterbody heat transfer rate is therefore expected to be minimal.

The dissociation reaction rates are a function of $\sqrt{TT_v}$ and may therefore be dependent on the thermal nonequilibrium state ($T \neq T_v$) on the afterbody. However, the large difference between $T$ and $T_v$ (see Fig. 11) is expected to have negligible effect on the chemical composition of the gas. This is because the species concentrations in the afterbody flowfield are frozen at levels corresponding to the forebody region. The low density that prevails downstream of the shoulder expansion inhibits any chemical reactions, irrespective of the thermal state of the gas. Thus, thermal nonequilibrium has minimal effect on the gas composition and therefore on the afterbody flow properties at the current conditions.

Figure 12 shows the distribution of eddy viscosity normalized by the local molecular viscosity. This ratio quantifies the effect of turbulence at each point in the domain. Eddy viscosity is negligible compared with molecular viscosity in the nose stagnation region. The boundary layer is initially laminar, and it becomes transitional with $\mu_T/\mu \simeq 5$ just upstream of the first corner. Strong flow expansion at the shoulder relaminarizes the boundary layer. Subsequently, there is a buildup of turbulence in the shear layer. In the recirculation region, $\mu_T \geq 20\mu$ and its value increases through the neck up to about $360\mu$ in the wake. The effect of turbulence on the flow predictions is discussed subsequently.

Figure 13 presents the computed surface properties on forebody of the vehicle. The wall pressure follows a parabolic profile with maximum at the nose stagnation point ($s/D = 0$) and a rapid drop due to expansion at the shoulder ($s/D = 0.52$). Heat transfer rate varies gradually on the forebody with a maximum value of 219 $\mathrm{W/cm^2}$ at the nose. The stagnation-point heating matches the theoretical estimate of Fay and Riddell [22] (shown by the symbol in Fig. 13b). At the expansion corner the heating rate has a local peak followed by a sharp decrease as the gas temperature drops due to flow expansion.

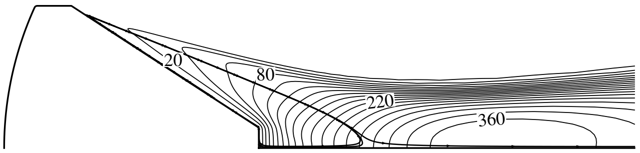

**Fig. 12 Normalized eddy viscosity distribution computed by turbulent (SA model) simulation. Representative streamlines are shown to identify the recirculation bubble.**

The pressure and heating rate on the afterbody surface are presented in Fig. 14. The vertical scales are magnified as compared with Fig. 13 to highlight the low afterbody levels. The extent of the conical frustum and flat base are identified in the figure. Flow expansion on to the conical afterbody results in a sharp decrease in pressure at $s/D \simeq 0.65$. A similar pressure drop due to the expansion of the reversed flow at the base corner is observed at $s/D \simeq 1.42$. The pressure at the base stagnation point is about 7.23 $p_\infty$, which is about 2% of the nose stagnation-point value. The expansion corners are also marked by local peaks in the heat transfer rate. Between the two expansion corners, the afterbody pressure and heating rate show a monotonic increase from the separation point at the shoulder to the base corner. The base stagnation-point heating rate is 22.48 $\mathrm{W/cm^2}$, which is 10.3% of the corresponding nose stagnation-point value.

The afterbody heating rate predicted by the SA model is found to exhibit small waviness along the conical frustum. This waviness occurs when the value of the damping function $f_w$ in the eddy viscosity equation drops below zero. The model equation with the damping function limited to nonnegative values results in a smooth variation of the afterbody heating rate, which is shown in Fig. 14b. This modification to the SA turbulence model does not affect any other part of the flow solution.

### A. Effect of Turbulence

To study the effect of turbulence on the flowfield, the preceding RANS flowfield is compared with the laminar solution computed at identical conditions. Figure 15 presents the temperature distribution and representative stream lines in the two cases. The forebody flowfield and the expansion around the shoulder are almost identical in the laminar and turbulent solutions. The main difference is in the afterbody flowfield. The laminar solution has a larger recirculation region than the turbulent case, which extends to a diameter downstream of the base. Also, in contrast to the turbulent solution, the reversed flow along the axis becomes supersonic in the laminar case. A normal shock is therefore formed at the base to slow the flow down to a subsonic Mach number before it reaches the rear stagnation point.

The laminar recirculation bubble is marked by multiple vortices originating from the primary, secondary, and tertiary separation points along the conical frustum. These vortices are found to oscillate, coalesce, and separate over time, resulting in an unsteady flow in this region. The size of the recirculation bubble and the location of the base shock are also found to oscillate in time. The laminar data presented in Fig. 15 correspond to a single time realization of the unsteady solution. The flow outside the wake is not affected much by the unsteady vortices and is found to be mostly

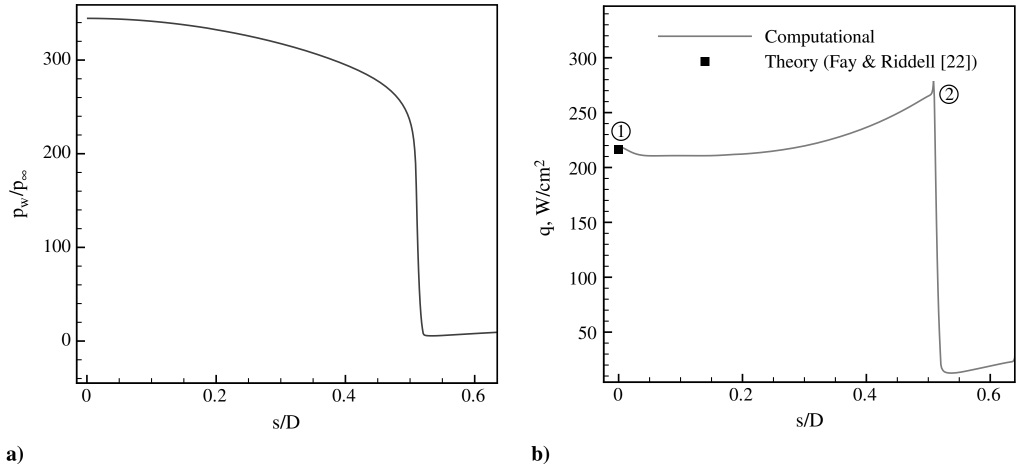

a) b)

**Fig. 13 Surface properties obtained using the SA turbulence model on the forebody: a) normalized pressure and b) heat transfer rate. Geometry points 1 and 2 are identified in Fig. 1c.**

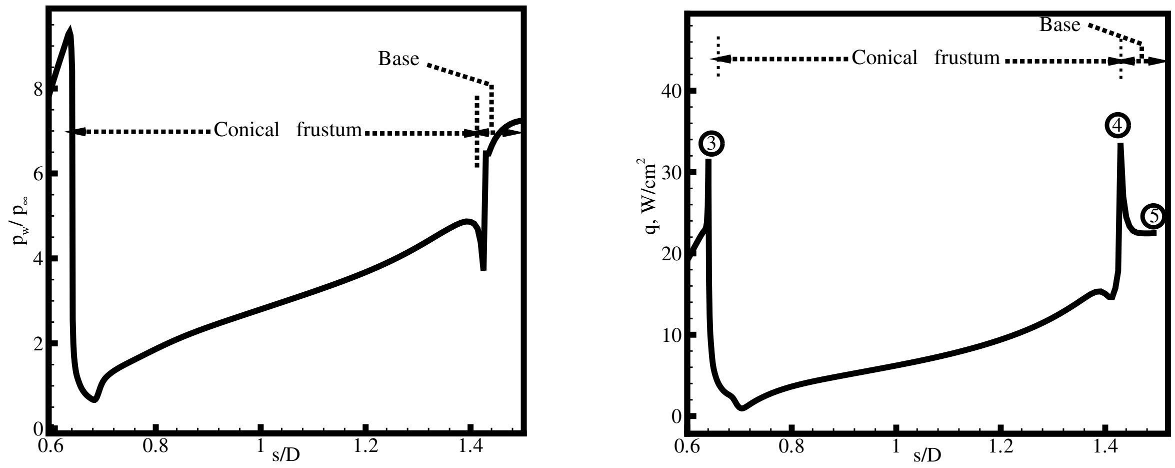

a) b)

**Fig. 14 Surface properties obtained using the SA turbulence model on the afterbody: a) normalized pressure and b) heat transfer rate. Geometry points 3, 4 and 5 are identified in Fig. 1c.**

steady. In the turbulent solution, the dominant effect of eddy viscosity ($\mu_T/\mu > 20$) dissipates the smaller vortices and increases the gas temperature. The turbulent recirculation bubble is much smaller, with peak temperature in the core region significantly higher than that in the laminar case.

Comparison of laminar and turbulent surface properties on the forebody is shown in Fig. 16. The turbulent heating rate deviates from the laminar value at $s/D \simeq 0.15$, marking the onset of transition. However, the difference between the two solutions is less than 28% because of the relatively low levels of eddy viscosity ($\mu_T/\mu < 6$) in the forebody boundary layer. The turbulence level decreases as the flow expands on to the shoulder, resulting in identical heating rates in the laminar and turbulent solutions immediately downstream of the first corner ($s/D = 0.52$). Further transition on the shoulder results in a higher heating rate (by up to 77% just before the second expansion corner) than in the laminar case. As expected, surface pressure distribution is not affected by transition to turbulence in the attached boundary layer on the forebody.

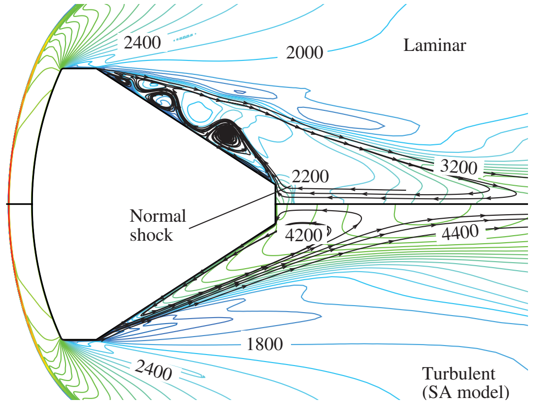

**Fig. 15 Comparison of temperature distribution and representative stream lines between laminar (top half) and turbulent (bottom half) flowfields.**

Afterbody surface pressure and heat transfer rate obtained from the laminar simulation (Fig. 17) have multiple peaks and minima. The low values of pressure correspond to vortex cores and the high-pressure regions are local flow separation and reattachment points. On the other hand, a low heat transfer rate is observed at flow separation points, and the reattachment points are marked by high local heating rates.

At the beginning of the separation bubble, pressure in the laminar solution is higher than the turbulent value. This is because of a smaller bubble in the turbulent case leading to larger flow expansion around the corner. Laminar pressure decreases along the frustum, whereas the turbulent pressure increases downstream such that their values are comparable on the later part of the conical afterbody. At the base, the presence of a normal shock in the laminar solution results in pressure level twice that in the turbulent case.

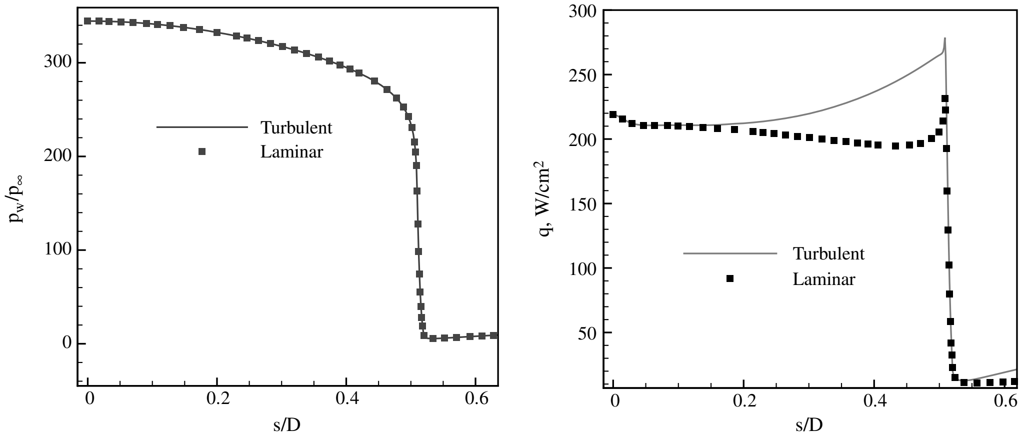

a) b)

**Fig. 16 Comparison of a) normalized pressure b) heat transfer rate in the laminar and turbulent solutions computed on the forebody.**

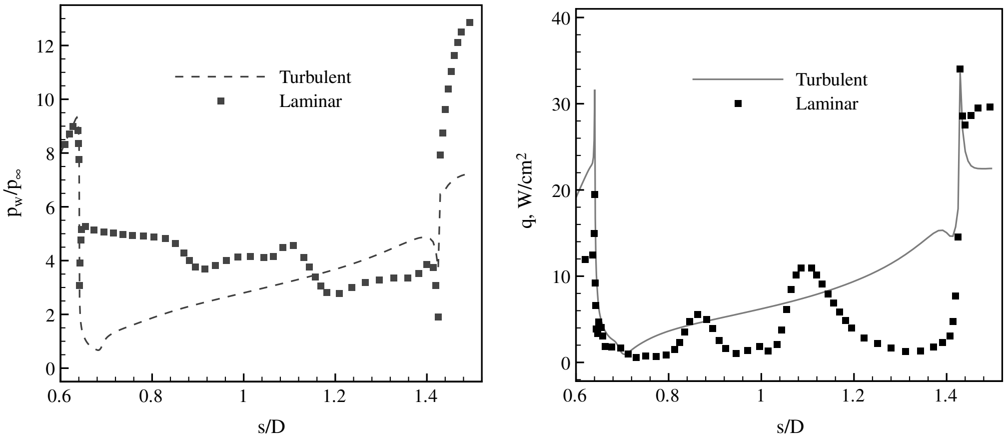

a) b)

Fig. 17 Comparison of a) normalized pressure b) heat transfer rate in the laminar and turbulent solutions computed on the afterbody.

The turbulent heat transfer rate (see Fig. 17b) increases along the afterbody from values comparable with the laminar case near the separation point to more than 5 times the laminar value at the end of the frustum. The only exceptions are the local flow-reattachment regions in the laminar solution. The higher heat transfer rate in the turbulent case is mainly because of higher temperature in the core of the recirculation bubble. With identical wall temperature in the laminar and turbulent solutions, a higher core temperature in the turbulent case yields a higher temperature gradient and therefore a higher heat transfer rate across the near-wall region. At the base, the laminar heat transfer rate increases drastically to 29.5 W/cm$^2$, due to the presence of the normal shock. It exceeds the turbulent value by 31.5%.

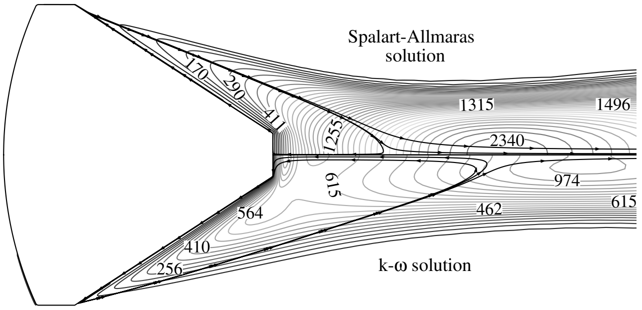

Fig. 18 Comparison of normalized eddy viscosity contours and separation bubble computed using the SA (top half) and *k-ω* (bottom half) turbulence models.

### B. Comparison of Turbulence Models

Wilcox's *k-ω* model [11] is used to compute the FIRE II flowfield, and the solution is compared with the SA model results presented previously. The grid-converged *k-ω* solution is obtained on a 240 × 191 computational grid with wall-normal spacing of $2.5 \times 10^{-7}$ m. This is equivalent to $y^+ = 0.25$ or lower along the entire vehicle. Adaptation of the afterbody grid to the free shear layer, similar to that of the SA model solution described earlier, is also carried out with identical results.

Figure 18 compares eddy viscosity levels in the two cases, with freestream molecular viscosity as a common reference for normalization. The *k-ω* model shows a faster buildup of eddy viscosity along the free shear layer compared with the SA solution. An opposite effect is seen downstream of the base, with $\mu_T$ in the SA solution exceeding the corresponding *k-ω* value by a factor of 2 or more. Lower eddy viscosity in the neck region makes the *k-ω* separation bubble larger by a factor of 2 than the SA solution. The separation point is also moved closer to the shoulder expansion corner, and the shear layer angle, measured with respect to the conical frustum, is increased by about 2 deg more than SA. As discussed in the laminar case, a larger separation bubble leads to lower flow expansion around the shoulder, thereby resulting in a higher pressure level on the conical afterbody in the *k-ω* solution than in SA (see Fig. 19). Forebody pressure computed using the two models is identical (see Fig. 20).

Afterbody heat transfer rate in the *k-ω* solution is higher than SA by 3–4 W/cm$^2$ along the conical frustum. The base heating is enhanced by about 44%. The difference in base heating predictions of the two models can be explained by studying the temperature and

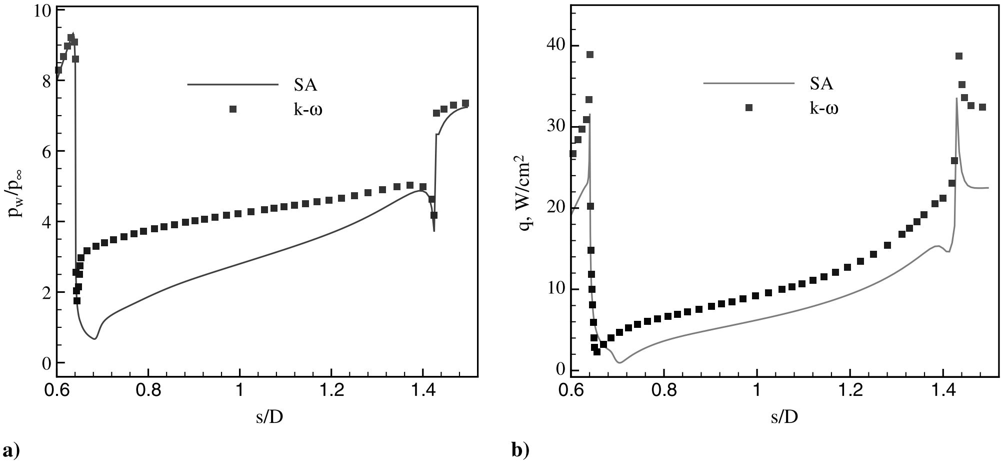

a) b)

Fig. 19 Surface properties obtained using the SA and *k-ω* turbulence models on the afterbody: a) normalized pressure and b) heat transfer rate.

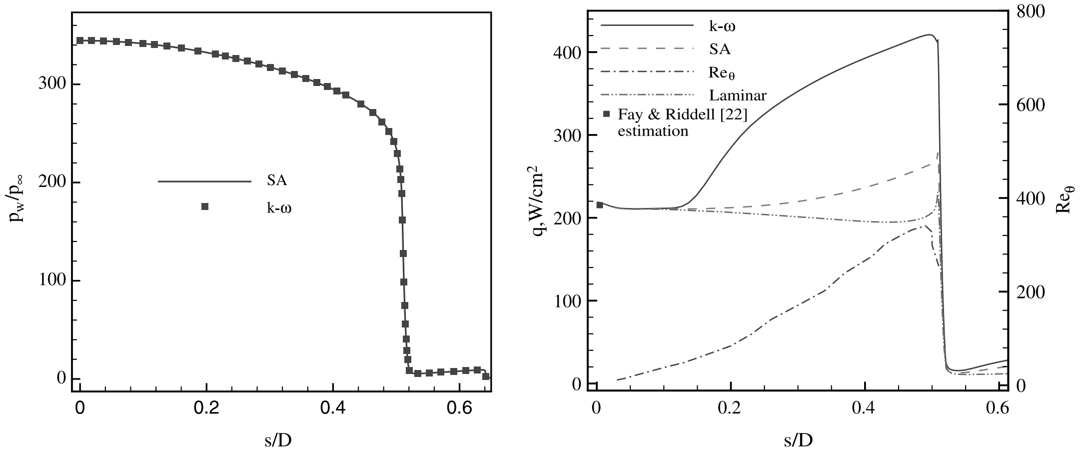

a) b)

**Fig. 20 Surface properties obtained using the SA and *k*-*ω* turbulence models on the forebody: a) normalized pressure and b) heat transfer rate and $Re_\theta$.**

eddy viscosity distribution along the base symmetry line (Fig. 21). The temperature at the neck is higher in the SA solution than *k*-*ω*, owing to the higher eddy viscosity and the resulting turbulent dissipation. An opposite trend is seen in the near-wall region, with *k*-*ω* eddy viscosity exceeding the corresponding SA value. The temperature gradient at the wall is determined by the eddy viscosity level in the vicinity of the wall. Therefore, the *k*-*ω* heating level is found to be higher than the SA prediction.

There are large differences between the forebody heating rate predictions by the two turbulence models (see Fig. 20). Unlike the gradual increase in heating rate predicted by the SA model, the *k*-*ω* solution gives a distinct jump in heat transfer rate at about $s/D = 0.12$. Compared with the SA results, the turbulent heating predicted by the *k*-*ω* model is significantly higher, with a peak heating (420 W/cm$^2$) about twice the stagnation-point value. Similar heating rate augmentation is experimentally observed on the CEV geometry by Hollis et al. [5].

Figure 20b also shows that $Re_\theta$ computed along the forebody boundary layer grows up to a value of 350 immediately before the expansion corner. The heating predictions of the two turbulence models deviate from the laminar value at $s/D = 0.12$, marking the onset of transition. This corresponds to $Re_\theta = 50$, which is significantly lower than the commonly used transition criterion of 200. Computation of transitional/turbulent flow on CEV forebody using an algebraic turbulence model exhibits a similar trend [5].

### C. Compressibility Corrections

The standard forms of turbulence models used previously were developed for incompressible flows. Several compressibility corrections are proposed in literature for their extension to high-speed flows. In two-equation models, compressibility corrections model the effect of dilatational dissipation [23] and pressure-dilatation correlation [24]. The net result is a reduction in the turbulent kinetic energy production and increase in the turbulent dissipation rate. Both of these lead to a reduced turbulence level in compressible mixing layers, thereby reducing the free-shear-layer growth rate compared with incompressible flows.

The compressibility correction proposed by Wilcox [25] is incorporated in the *k*-*ω* model, and the computed results are compared with the baseline *k*-*ω* solution. Normalized turbulent kinetic energy contours plotted in Fig. 22 show the reduction in turbulence level (by about 50%) due to the compressibility corrections. A similar decrease in the eddy viscosity levels is also observed between the two solutions. The majority of the reduction is in the free shear layer and the neck region, and it increases the separation bubble size in the compressibility-corrected *k*-*ω* solution. This in turn enhances the surface pressure on a significant portion of the conical frustum, compared with the baseline *k*-*ω* prediction (see Fig. 23a).

The temperature level in the recirculation region is comparable in the two solutions. The resulting heat transfer rates are almost identical over the majority of the conical frustum (see Fig. 23b). The difference in the base heating value is caused by a higher reverse

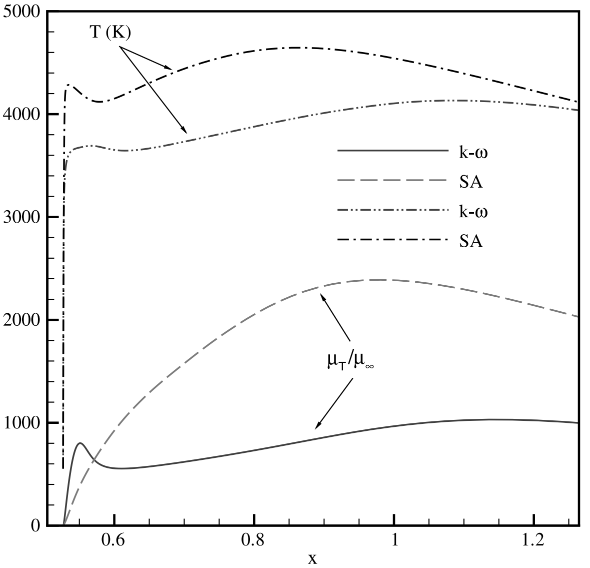

**Fig. 21 Comparison of normalized eddy viscosity and temperature along wake symmetry axis between SA and *k*-*ω* model. The location $x = 0.53$ corresponds to the base stagnation point.**

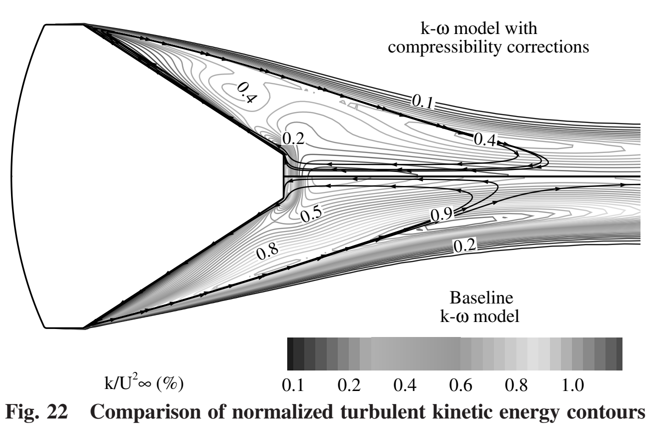

**Fig. 22 Comparison of normalized turbulent kinetic energy contours and separation bubble between *k*-*ω* (bottom half) and compressibility-corrected *k*-*ω* model (top half).**

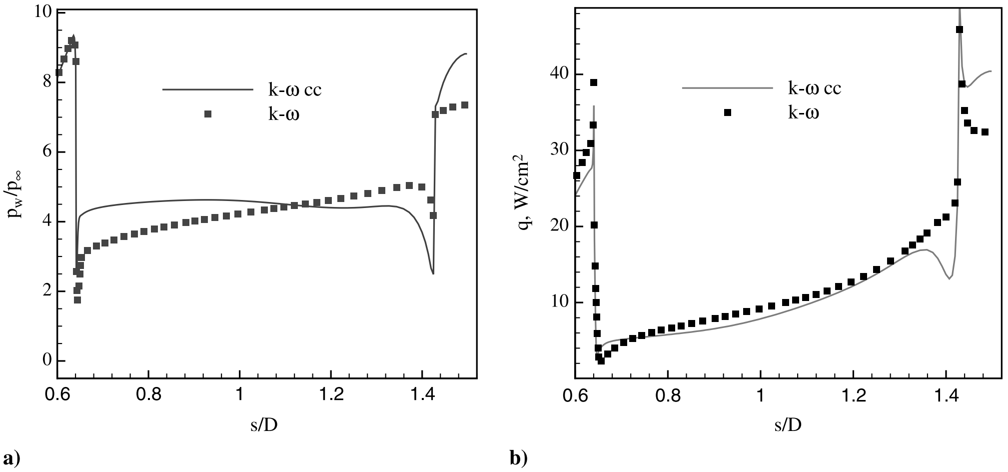

**Fig. 23** **Effect of compressibility corrections (denoted by cc) on *k*-*ω* turbulence model afterbody predictions: a) surface pressure b) heat transfer rate.**

velocity along the wake symmetry line for the compressibility-corrected model. In this case, the flow approaching the base stagnation point reaches up to Mach 0.91, as compared with a maximum Mach number of 0.55 in the baseline *k*-*ω* solution. This also results in a higher base pressure in the solution computed using the compressibility corrections.

For the SA turbulence model, Paciorri and Sabetta [26] propose a Mach-number-based modification to the production of eddy viscosity in the model equation. This decreases the eddy viscosity level in compressible mixing layers and thus reduces their spreading rate. Shur et al. [27] achieve a similar reduction in spreading rate by adding a negative source term to the eddy viscosity equation. The compressibility corrections to the SA model have an effect similar to the *k*-*ω* results discussed previously. The surface pressure is elevated compared with the baseline model. In addition, the heat transfer rate is reduced compared with the standard SA model.

Based on the comparison with flight data presented subsequently, compressibility corrections are expected to have a detrimental effect on the turbulence model predictions, especially for the surface pressure. This is in contrast to the findings in [28], in which the compressibility corrections improved results for supersonic base flows. This is probably because the Reynolds number in the current simulations is about an order of magnitude lower than that in the base flow calculations by Forsythe et al. [28]. Compressibility corrections may not be required at these low Reynolds number conditions and therefore are not pursued further.

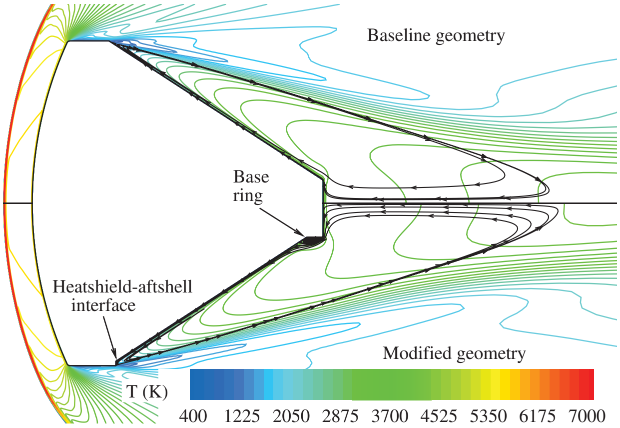

**Fig. 24** **Comparison of temperature contours and separation bubble between baseline geometry (top half) and modified geometry (bottom half) using the *k*-*ω* model.**

### D. Effect of Geometric Simplifications

The FIRE II vehicle geometry has ringlike structures at the heatshield/aftshell interface and at the base corner. The simplified geometry presented previously does not include these details. An updated outer mold line is simulated to study the effect of these additional geometrical features, if any, on the computed flow predictions. The exact dimensions of these ringlike structures could not be found in the literature. Their sizes are approximated from geometry sketches given in [29] and they are modeled as finite height steps at the respective locations (see Fig. 24).

The finite step at the beginning of the conical afterbody moves the separation point upstream to the corner location. A small secondary vortex (see Fig. 25a) is formed close to the separation point.

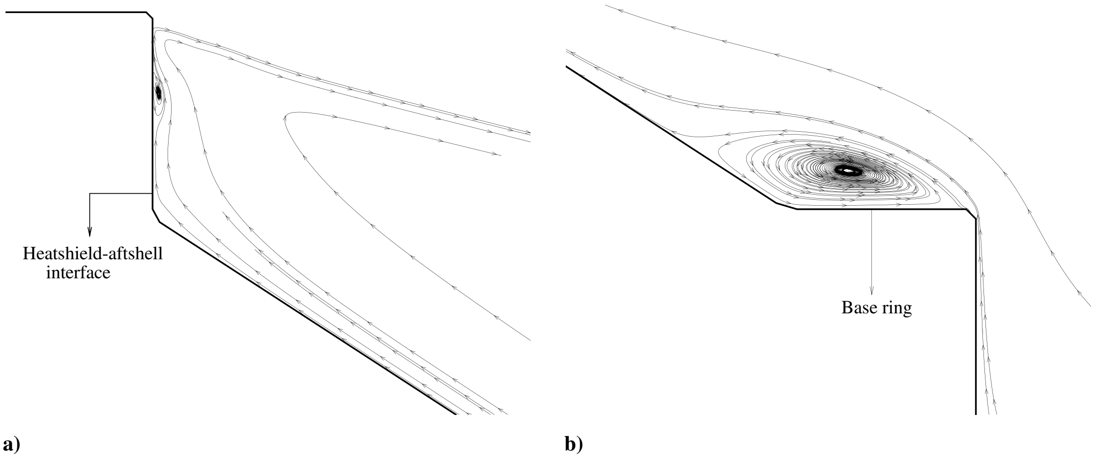

**Fig. 25** **Enlarged view of secondary flow separation regions in the flowfield over modified geometry model a) heat-shield/aftshell interface b) base ring.**

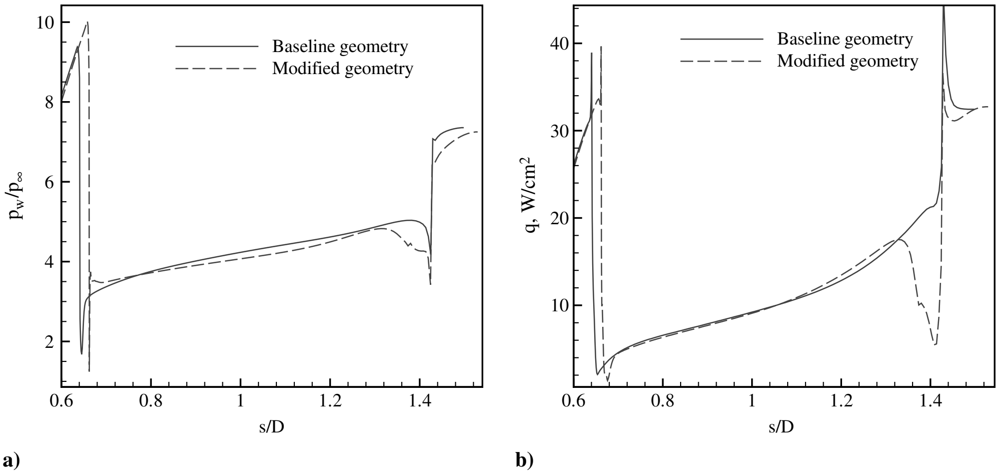

**Fig. 26 Effect of heat-shield/aftshell interface and base ring on surface properties: a) normalized pressure b) heat transfer rate.**

Secondary separation is also observed at the base ring (see Fig. 25b). In spite of these changes, the overall size of the recirculation bubble and the shear layer angle are found to be comparable with the baseline geometry (Fig. 24).

The surface pressure and heat transfer rates computed using the modified geometry are close to that of the baseline geometry over majority of the conical frustum (Fig. 26). The only differences are localized in the regions of geometry variation. The finite step at the heat-shield/aftshell interface is found to increase the surface pressure in this region. On the other hand, the secondary vortex at the base corner reduces the surface pressure and heating rate. There is a negligible effect of the geometry variations on the heat transfer prediction in the range $0.7 < s/D < 1.3$, in which comparison is made with the in-flight measurements.

### E. Comparison with Flight Data

The pressure and heating rate measured during flight are compared with the different computational results in Fig. 27. Pressure is measured at $s/D = 1.27$, and surface heating values are available at $s/D = 0.77$, 0.96, 1.13, and 1.27. For a fixed axial station, there is little variation between the heating data at different circumferential locations. Therefore, the heat transfer rates along the three circumferential rays ($\phi = 0$, 120, and 240 deg) are not distinguished in Fig. 27b.

Experimental measurements in turbulent base flow yield uniform pressure in the separation bubble [30]. This may be because of the unsteady turbulent mixing in the core flow that helps in equalizing the pressure on the base and thus yields a uniform surface pressure in the time-averaged solution. A similar trend is expected to be valid in the turbulent recirculation bubble at the current conditions, and therefore the single pressure data point is taken as representative of the entire conical frustum. This is indicated by the dotted line in Fig. 27a. The in-flight measurement is lower than all the different computations, with the SA turbulence model predictions being the closest over majority of the conical frustum. The *k*-*ω* results are appreciably higher. Laminar simulation yields the highest pressure near the separation point and it predicts one of the lowest values in the later part of the conical frustum.

There is large scatter in the pressure measurement between the range 1651.75 and 1655.75 s, which brackets the current trajectory point. This is because the afterbody pressure levels during this period are close to the upper operating limit of the pressure sensing system. The actual afterbody pressure may therefore be higher than the value reported in [7]. A higher in-flight pressure level is expected to improve the comparison between computation and measurement.

Comparing the heating rate data in Fig. 27b, we see that the laminar results are far lower than flight data, except for the local peaks in heat transfer. Even an average value will considerably underpredict the in-flight measurements. By comparison, RANS results are closer to the data, with values lower than measurement at the beginning of the recirculation bubble. Both SA and *k*-*ω* model predictions monotonically increase to exceed the flight data in the later part of the conical frustum.

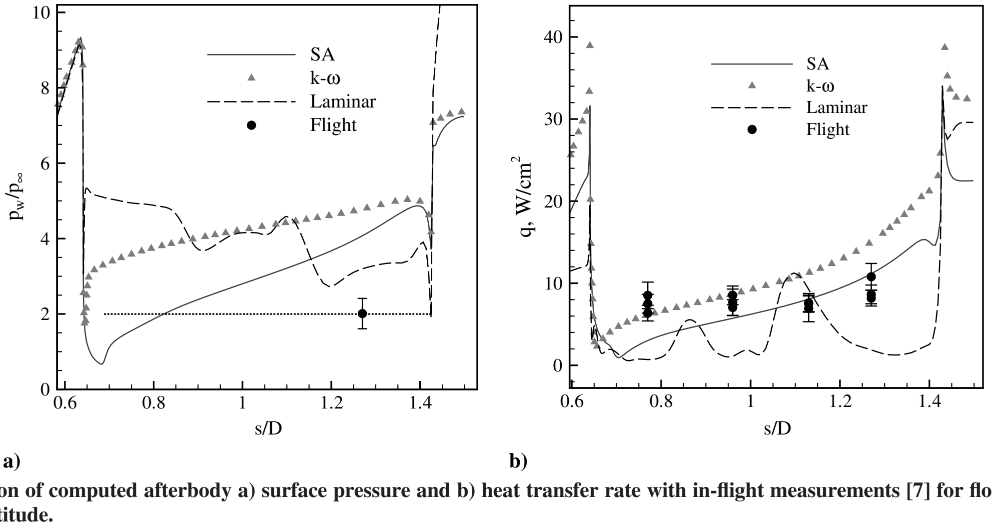

**Fig. 27 Comparison of computed afterbody a) surface pressure and b) heat transfer rate with in-flight measurements [7] for flow over the FIRE II capsule at 35 km altitude.**

## V. Conclusions

Hypersonic turbulent flow around the FIRE II reentry module is computed using the Reynolds-averaged Navier–Stokes method. Five-species air chemistry and a two-temperature vibrational relaxation model is used in the simulations. Turbulence closure is achieved using the one-equation Spalart–Allmaras (SA) and two-equation $k$-$\omega$ models. The standard forms of the model equations are used in the computation. Compressibility corrections are not found to improve prediction over the baseline models.

The boundary-layer flow on the forebody transitions to turbulence, with large discrepancy between the turbulent heating levels predicted by the two turbulence models. Also, the computed transition location is upstream of that given by usually accepted transition criteria. On the afterbody, there are large differences in the eddy viscosity level in the neck region between the two models. This has a dominant influence on the size of separation bubble, shear layer angle, and surface pressure value. The SA solution has a much lower afterbody pressure than the $k$-$\omega$ model. Both turbulence models are found to overpredict the in-flight pressure measurements significantly. Discrepancy in the afterbody heating rate is much lower, with the two turbulence models predicting comparable temperature levels in the recirculation-bubble core flow. Higher eddy viscosity in the $k$-$\omega$ solution in the near-wall region, however, yields a slightly higher heating rate on the frustum and base than the SA solution. On the whole, both models are found to predict the in-flight heating measurements reasonably well.

## Acknowledgments

The authors would like to thank the reviewer for his/her extensive comments that have helped in improving the manuscript significantly. The authors also thank Indian Space Research Organization (ISRO) for supporting this research under the RESPOND programme.

## References

[1] Wright, M. J., Milos, F. S., and Tran, P., "Afterbody Aeroheating Flight Data for Planetary Probe Thermal Protection System Design," *Journal of Spacecraft and Rockets*, Vol. 43, No. 5, Sept.–Oct. 2006, pp. 929–943.
doi:10.2514/1.17703

[2] Schneider, S. P., "Laminar-Turbulent Transition on Reentry Capsules and Planetary Probes," *Journal of Spacecraft and Rockets*, Vol. 43, No. 6, Nov.–Dec. 2006, pp. 1153–1173.
doi:10.2514/1.22594

[3] Wright, M. J., Loomis, M., and Papadopoulos, P., "Aerothermal Analysis of the Project FIRE II Afterbody Flow," *Journal of Thermophysics and Heat Transfer*, Vol. 17, No. 2, Apr.–June 2003, pp. 240–249.
doi:10.2514/2.6757

[4] Wright, M. J., Prabhu, D. K., and Martinez, E. R., "Analysis of Apollo Command Module Afterbody Heating Part 1: AS-202," *Journal of Thermophysics and Heat Transfer*, Vol. 20, No. 1, Jan.–Mar. 2006, pp. 16–30.
doi:10.2514/1.15873

[5] Hollis, B. R., Berger, K. T., Horvath, T. J., Coblish, J. J., Norris, J. D., Lillard, R. P., and Kirk, B. S., "Aeroheating Testing and Predictions for Project Orion CEV at Turbulent Conditions," AIAA Paper 2008-1226, 2008.

[6] Brown, J. L., "Turbulence Model Validation for Hypersonic Flows," AIAA Paper 2002-3308, 2002.

[7] Slocumb, T. H., "Project Fire Flight II Afterbody Temperatures and Pressures at 11.35 Kilometers Per Second," NASA TM X-1319, 1966.

[8] Lees, L., "Hypersonic Wakes and Trails," *AIAA Journal*, Vol. 2, No. 3, Mar. 1964, pp. 417–428.
doi:10.2514/3.2356

[9] Park, C., *Non-Equilibrium Hypersonic Aerothermodynamics*, Wiley-Interscience, New York, 1990.

[10] Millikan, R. C., and White, D. R., "Systematics of Vibrational Relaxation," *Journal of Chemical Physics*, Vol. 39, No. 12, 1963, pp. 3209–3213.
doi:10.1063/1.1734182

[11] Wilcox, D. C., "Reassessment of the Scale Determining Equation for Advanced Turbulence Models," *AIAA Journal*, Vol. 26, No. 11, Nov. 1988, pp. 1299–1310.
doi:10.2514/3.10041

[12] Spalart, P. R., and Allmaras, S. R., "A One-Equation Turbulence Model for Aerodynamic Flows," AIAA Paper 92-0439, 1992.

[13] Blottner, F. G., Johnson, M., and Ellis, M., "Chemically Reacting Viscous Flow Program for multicomponent Gas Mixtures," Sandia Labs. Rept. SC-RR-70-754, Albuquerque, NM, 1971.

[14] Vincenti, W. G., and Kruger, C. H., *Introduction to Physical Gas Dynamics*, Krieger, Malabar, FL, 1986.

[15] Wilke, C. R., "A Viscosity Equation for Gas Mixtures," *Journal of Chemical Physics*, Vol. 18, 1950, pp. 517–519.
doi:10.1063/1.1747673

[16] Palmer, G. E., and Wright, M. J., "Comparison of Methods to Compute High-Temperature Gas Viscosity," *Journal of Thermophysics and Heat Transfer*, Vol. 17, No. 2, Apr.–June 2003, pp. 232–239.
doi:10.2514/2.6756

[17] MacCormack, R. W., and Candler, G. V., "The Solution of the Navier–Stokes Equations Using Gauss-Seidel Line Relaxation," *Computers and Fluids*, Vol. 17, No. 1, 1989, pp. 135–150.
doi:10.1016/0045-7930(89)90012-1

[18] Sinha, K., and Candler, G. V., "Convergence Improvement of Two-Equation Turbulence Model Calculations," AIAA Paper 98-2649, 1998.

[19] Wright, M. J., Candler, G. V., and Bose, D., "Data-Parallel Line Relaxation Method for the Navier–Stokes Equations," *AIAA Journal*, Vol. 36, No. 9, 1998, pp. 1603–1609.
doi:10.2514/2.586

[20] Menter, F. R., "Two-Equation Eddy-Viscosity Turbulence Models for Engineering Applications," *AIAA Journal*, Vol. 32, No. 8, 1994, pp. 1598–1605.
doi:10.2514/3.12149

[21] Sinha, K., "Reynolds-Averaged Navier–Stokes Simulation of FIRE II Reentry Configuration," *25th International Symposium on Shock Waves*, Indian Inst. of Science, Bangalore, India, 2005.

[22] Fay, J. A., and Riddell, F. R., "Theory of Stagnation Point Heat Transfer in Dissociated Air," *Journal of the Aeronautical Sciences*, Vol. 25, No. 2, Feb. 1958, pp. 73–85.

[23] Sarkar, S., Erlebacher, G., Hussaini, M. Y., and Kreiss, H. O., "The Analysis and Modeling of Dilatational Terms in Compressible Turbulence," *Journal of Fluid Mechanics*, Vol. 227, 1991, pp. 473–493.
doi:10.1017/S0022112091000204

[24] Sarkar, S., "The Pressure Dilatation Correlation in Compressible Flows," *Physics of Fluids*, Vol 4, 1992, pp. 2674–2682.
doi:10.1063/1.858454

[25] Wilcox, D. C., *Turbulence Modeling for CFD*, 2nd ed., DCW Industries, Inc., La Cañada, CA, 1998, pp. 244–245.

[26] Paciorri, R., and Sabetta, F., "Compressibility Correction for the Spalart–Allmaras Model in Free-Shear Flows," *Journal of Spacecraft and Rockets*, Vol. 40, No. 3, 2003, pp. 326–331.
doi:10.2514/2.3967

[27] Shur, M., Strelets, M., Zaikov, L., Gulyaev, A., Kozlov, V., and Secundov, A., "Comparative Numerical Testing of One- and Two-Equation Turbulence Models for Flows with Separation and Reattachment," AIAA Paper 95-0863, 1995.

[28] Forsythe, J. R., Hoffmann, K. A., and Squires, K. D., "Detached-Eddy Simulation with Compressibility Corrections Applied to a Supersonic Axisymmetric Base Flow," AIAA Paper 2002-0586, 2002.

[29] Richardson, N. R., "Project FIRE Instrumentation for Radiative Heating and Related Measurements," NASA TN D-3646, 1966.

[30] Bourdon, C. J., Smith, K. M., Dutton, J. C., and Mathur, T., "Planar Visualization of Large Scale Turbulent Structures in Axisymmetric Supersonic Base Flows," AIAA Paper 98-0624, 1998.

G. Palmer
*Associate Editor*